# Structural and corrosion properties of SiC-NiCr nanocomposite coating on Zr substrate in high temperature

Hasan Anousha[1], Shervin Goudarzi[2], Mohammad Esmailpour[1]*, Dariush Rostamifard[2]

[1]*Department of Physics, Azarbaijan Shahid Madani University, Tabriz, Iran.*
[2]*Nuclear Science and Technology Research Institute, Atomic Energy Organization of Iran, Tehran, Iran.*

**Corresponding author**: esmailpour201020@gmail.com

**Abstract:**

The present report describes the deposition of SiC-NiCr films on Zr substrates under an $H_2$ gas environment by plasma focusing (PF). Using the spark plasma sintering (SPS) method, the anode for the plasma focus device was made from SiC, Ni, and Chromium powders. X-ray diffraction (XRD) of SiC-NiCr samples shows a change in the position and intensity of the peaks in 1000 °C temperature compared to the XRD spectrum at room temperature (RT). The surface characteristics and structure of the synthesized coating were investigated with Field Emission Scanning Electron Microscopy (FESEM) at RT and 1000 °C. According to the FESEM images, the average coating nanoparticles size increases from 58.2 nm to 326.6 nm, and the average coating thickness increases from 0.85 $\mu$m to 60.34 $\mu$m by increasing the temperature. At high temperatures, the thermogravimetric analysis (TGA) of samples indicates a reduction in corrosion rate from 3.25 to 0.22 mg/cm$^2$. The coating of Zr with a thin layer of SiC-NiCr is capable of preventing or reducing the possibility of hydrogen explosions in extreme conditions.

**Keywords:** Zirconium; SiC–NiCr; Plasma Focus; XRD; FESEM; TGA

## 1. Introduction

Following the Fukushima nuclear accident, Zr based alloys were found to lose their integrity under critical conditions [1–3]. High temperature reactions of zirconium (Zr) and water result in large quantities of hydrogen gas being released [4, 5]. Due to their high strength and corrosion resistance in the cooling environment, zirconium alloys are used for the production of nuclear fuel pellets [6]. After the 2011 Japan Earthquake and Tsunami, there was considerable interest worldwide in developing fuel pellets that perform better in rare situations [7–11]. In the event of a loss of coolant accident (LOCA), fuel cladding can be subjected to the most critical conditions [12, 13]. The loss of pressure in the nuclear core and the coolant vaporization can result in LOCA events if the primary cooling system breaks down. In these conditions, the temperature of the fuel rises, increasing the porosity of the fuel and fragmentation of the material. A sudden increase in fuel cladding temperature is also observed. By releasing additional heat due to the exothermic reaction, Zr based claddings interact with steam at high temperatures (above 800 °C) and cause oxidation and embrittlement:

Zr (s) + 2H$_2$O (1) → ZrO$_2$ (s) + 2H$_2$ (g) + 584.5 kJ/mol
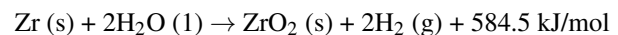
A practical solution to this problem is the development of protective coatings on the surfaces of Zr fuel sheaths [14, 15]. The protective coating should reduce the hydrogen absorption of Zr based alloys in reactors, improve corrosion resistance, and protect against high-temperature oxidation [16–18]. Since silicon carbide has an excellent corrosion resistance and a similar thermal neutron capture cross−section to zirconium, it is one of the primary options for protecting or replacing fuel claddings [19–22]. Using a magnetron sputtering system, M. J. Suriani et al. produced an amorphous SiC coating by depositing silicon
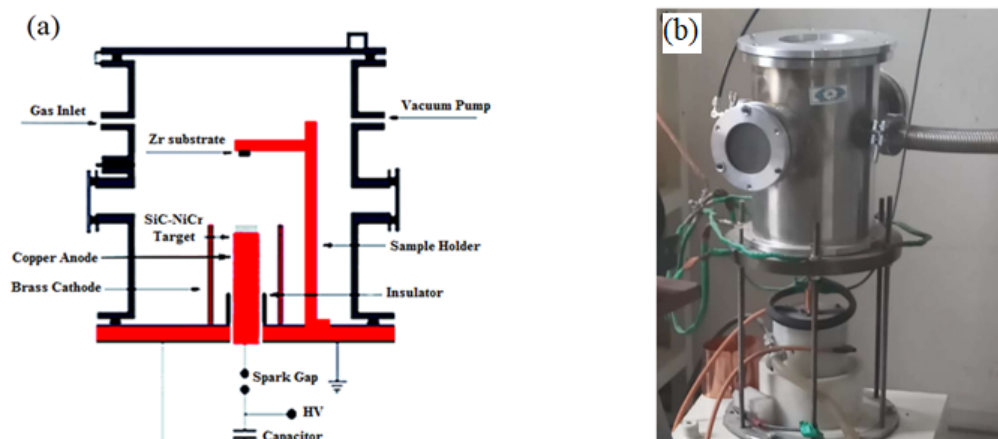
**Figure 1.** a) Schematic of Mather plasma focus device and b) Image of the plasma focus device used in the research.

carbide (SiC) films on stainless steel. For periods of prolonged immersion, metals that have not been coated lose more weight than metals that have been coated [23]. As a result of the use of a Mather type dense plasma focus device with a 20 kJ utility, Z.P. Wang et al. were able to grow silicon carbide (SiC) films on a silicon substrate [24]. Using DC magnetron sputtering of composite cathodes, 1.5 $\mu$m thick amorphous SiC coatings were deposited on zirconium alloy substrates [25]. R. Schmid and K. Bhanumurthy analyzed bulk diffusion pairs of SiC with Cr, Zr, and Ni metals at temperatures ranging from 700 ºC-1300 ºC to determine the interfacial reactions. Complex structures are formed in the reaction zone as a result of interface reactions. SiC/Ni interface reactions produce periodic bands, whereas SiC/Cr and SiC/Zr produce layered structures. As a result of the present investigation, it has been found that the main diffusing species in the SiC/Cr and SiC/Zr couples are C and metal atoms. Carbon has almost no mobility in diffusion couples based on SiC/Ni [26]. The electron deposition method was used to prepare nanocomposite coatings from nickel on pure copper samples by Mansour Hashem et al. who realized that nickel-chromium, nickel-silicon,

and carbide-chromium coatings with chromium and silicon-carbide particles increases the microhardness and wear resistance [27]. Deposition of metal matrix composites (MMCs) consisting of carbides, metals and, some other materials is a flexible and low-cost method for composite coating. New composite SiC-NiCr films have shown better mechanical, tribological, anti-corrosion and anti-oxidation properties compared to the pure metal coatings.

In this study, according to the purpose of the research, zirconium was used as a substrate due to its low neutron absorption cross section in nuclear applications. We chose the PF method because chemical reactions are reduced and the prepared coatings are more resistant to corrosion compared to other coating processes such as electro deposition. We select the SiC-NiCr coating because of its remarkable properties including low hydrogen absorption coefficient, hardness and excellent corrosion resistance, which is a critical feature for the Zr substrate at high temperatures to prevent hydrogen embrittlement [28]. Due to the short duration and high ion density, PF discharge produce plasmas with high ion density that, after exposure to a high energy density, cause the anode (SiC-NiCr) to be pulverized and produce a vapor that can be rapidly deposited [29, 30]. As far as we know, the present study is the first to investigate the spectroscopy of
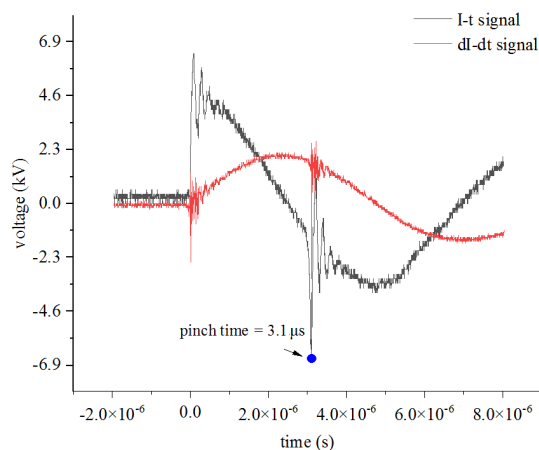


**Figure 2.** Rogowski coil current derivative signal at pinch time.
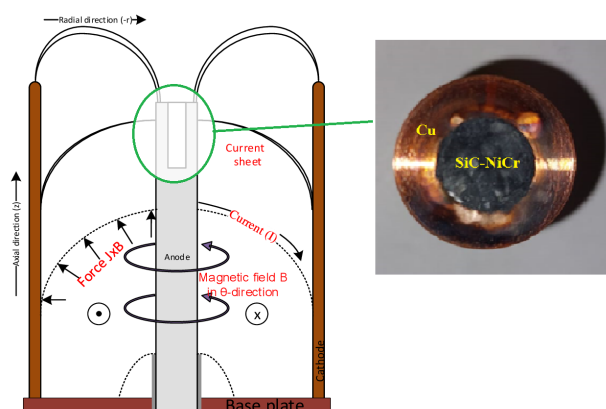


**Figure 3.** Performance of plasma focus device.

**Table 1.** Specifications of the SPS device.

| | |
|---|---|
| Maximum temperature ($^o$C) | 2200 |
| Vacuum (torr) | $10^{-2}$ |
| Voltage (V) | 20 |
| Maximum current power (kA) | 10 |
| Maximum pressure (Torr) | 60 |
| Power supply | DC pulse |
| Frequency (Hz) | 200 |

**Table 3.** XRD results of a structural SiC−NiCr thin film.

| Sample $^o$C | Micro strain | Crystal dislocation ($\times 10^{-3}$) | Crystallite size (nm) |
|---|---|---|---|
| 25 | 0.29 | 0.44 | 47.2 |
| 1000 | 0.19 | 0.23 | 65.08 |

SiC-NiCr nanocomposite coatings that are plasma focused. SiC-NiCr coating was grown on a Zr substrate using a PF device. An analysis of the structural and corrosion behavior of SiC-NiCr cermets produced at high temperatures is presented in this paper. XRD, FESEM and AFM were used to investigate the structure and surface topography of the synthesized samples, while thermogravimetric analysis was used to evaluate their corrosion properties.

## 2. Material and Methodology

A 2 kJ Mather type plasma focus device was used in this experimental study to deposit SiC-NiCr coatings. Zr was used as a substrate with dimensions of 10 mm×10 mm×1 mm. It is important to note that the used PF device has a 39 $\mu$F capacitor bank, which can be further charged up to 12 kV. There are twelve brass cathode electrodes, each measuring 10 mm in diameter and 145 mm in height, around the copper anode electrode, which measures 29 mm in diameter and 95 mm in length. The electrodes are separated by a pyrex insulator with a height of 50 mm.

The schematic of the plasma focus device and the image of the PF device used in the research are shown in figure 1. Anode was prepared using silicon carbide, chromium, and nickel powders (99.9% purity) at weight ratios of 100, 80, and 20 gr, respectively, using a spark plasma sintering (SPS) procedure. An SPS process involves the creation of a powder. During this process, powder materials are heated within a furnace at a temperature below their melting point. Thus, the atoms move within the powder particle (infiltrate), and the bond between them is formed. Table 1 contains the specifications of the SPS device used. A rotary compressor lowered the pressure of the entire electrode set to 0.2 torr within a vacuum container. Afterward, H$_2$ gas was injected

**Table 2.** The deposition conditions of the prepared SiC-NiCr coating.

| | |
|---|---|
| Effective length of the anode (mm) | 95 |
| Anode diameter (mm) | 29 |
| Effective insulation height (mm) | 50 |
| Cathode rod height (mm) | 145 |
| Cathode rod diameter (mm) | 10 |
| Number of cathode rods | 12 |
| Anode to substrate distance (mm) | 46.5 |
| Number of shots | 20 |
| Optimal voltage (kV) | 12 |

into the vacuum container. An optimal pressure of 0.2 torr at a voltage of 12 kV was found to be optimal for an excellent pinch in the experiment. An oscilloscope was used to record the voltage in terms of the current waveform at pinch time received from the Rogowski coil (Fig. **??**). An electrostatic field was applied between the anode and cathode by means of a 39 $\mu$F capacitor recharged by a high voltage in order to operate the PF device. The surface of the insulator was then affected by an electrical discharge, resulting in layer of current on it. Lorentz force is created when a self−consistent magnetic field is created to accelerate the current layer toward the anode's open end. This resulted in compression of the anode's current layer, creating heated dense plasma. The elimination of the plasma column generated a strong magnetic field, which must be noted. A collision between high−energy electrons and the anode occurred when the electrons and ions were accelerated in opposite directions (Fig. 3). Samples were placed 46.5 mm above the anode. Table 2 shows the deposition conditions for the prepared SiC-NiCr coating.

XRD, FESEM, AFM, and TGA were also conducted on the SiC−NiCr coating placed at 0$^o$ relative to the anode axis with 20 shots. The XRD (PHILIPS PW1730) with Cu$_{K\alpha}$ radiation of wavelength 1.5406 Å at a generator setting of 30 mA and 40 kV in the 2$\theta$ range from 10$^o$ to 80$^o$ and step size 0.05$^o$ was used to obtain the structure of the SiC−NiCr thin films. Using FESEM, the surface morphology of the coating was analyzed (MIRA 3 TESCAN). An AFM (Nanosurf Mobile S) was used to measure the roughness of the surface. TGA charts were recorded using the SDT Q600 TA differential thermal analysis device.

## 3. Structural properties

### 3.1 Grazing incidence X-ray diffraction (GIXRD)

X−ray diffraction spectrum of SiC-NiCr coatings at RT and 1000 $^o$C by grazing technique is shown in Figure 4. In

**Table 4.** Parameters of the misfit strain and misfit stress.

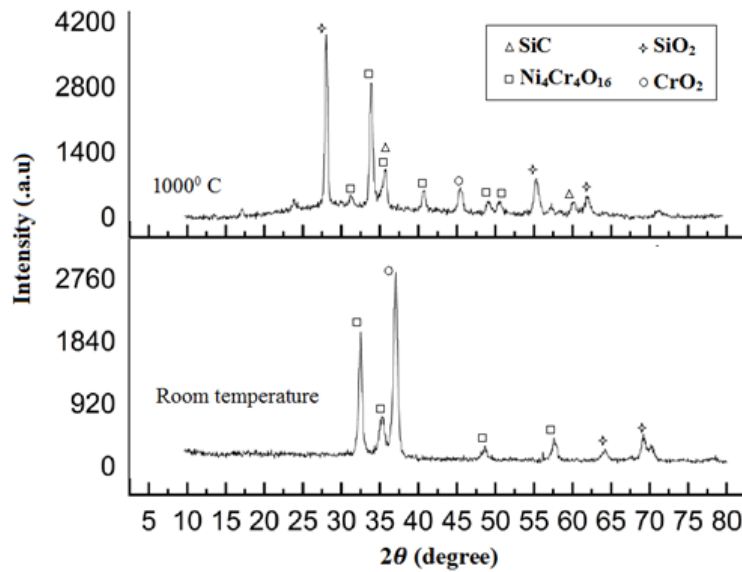| | |
|---|---|
| b$_f$ ($\times 10^{-6}$/K) | 9.65 |
| b$_s$ ($\times 10^{-6}$/K) | 7.20 |
| $\varepsilon_0$ ($\times 10^{-3}$) | 2.30 |
| E$_f$ ($\times 10^2$ (Gpa) | 2.045 |
| v$_f$ | 0.30 |
| $\sigma_0$ (Gpa) | 0.67 |

**Figure 4.** X-ray diffraction patterns at room temperature and 1000 ºC.

this method, the incident X−ray beam strike the sample at a very small angle ($\leq 50^{\circ}$) and analyzes the scattered X ray beams of the surface structure. The peaks related to diffraction $Ni_4Cr_4O_{16}$ were observed in the angles of $32.64^{\circ}$, $35.17^{\circ}$, $42.21^{\circ}$, $48.67^{\circ}$, $51.16^{\circ}$, $53.43^{\circ}$, and $57.94^{\circ}$, assigned to (200), (112), (221), (113), (310), (311), and (241), crystallographic planes, respectively, according to the JCPDS PDF no. 96−100−8083. Also, at 1000ºC, the spectra of the film deposited show two diffraction SiC peaks at $35.73^{\circ}$ and $60.14^{\circ}$ assigned to (111) and (022) crystallographic planes, respectively, according to the JCPDS PDF no. 96−900−8857 (Fig. 4).

The average sizes of the crystallites $D$, crystal dislocation $\delta$, and micro strain $\varepsilon$ were estimated from the main reflections of the XRD and were calculated by the following relations (1), (2), and (3). [29]

$$D = \frac{K\lambda}{\beta \cos \theta} \tag{1}$$

$$\delta = \frac{1}{D^2} \tag{2}$$

$$\varepsilon = \frac{\beta \cos \theta}{4} \tag{3}$$

where $k$ is the shape factor ($k$=0.94), $\lambda$ is the wavelength of the applied X-ray ($\lambda_{CuK\alpha}$=0.154056 nm), $\theta$ is the Bragg's angle, and $\beta$ is the pure diffraction line broadening (in radians), which can be found by measuring the full width at the half maximum (FWHM). Table 3 illustrates the XRD results of a structural SiC-NiCr thin film on the Zr substrate. According to Table 3, the crystallite size increases at 1000ºC temperature. Also, the crystal dislocation and as a result the microstrain of the SiC-NiCr coating is reduced compared to room temperature.

## 3.2 Field emission scanning electron microscopy (FE-SEM)

A FESEM was used to determine the morphology of the nanoparticles prepared. A description of the surface morphology of the SiC−NiCr layer on Zr is provided in Figs. 5a and b. An island−layer structure is formed by coating nanoparticles (Stranski–Krastanov growth). An island−layer growth process involves the formation of
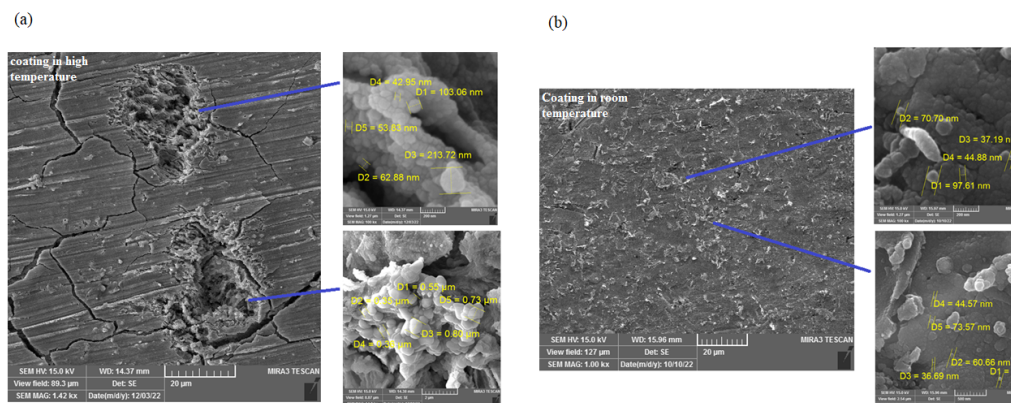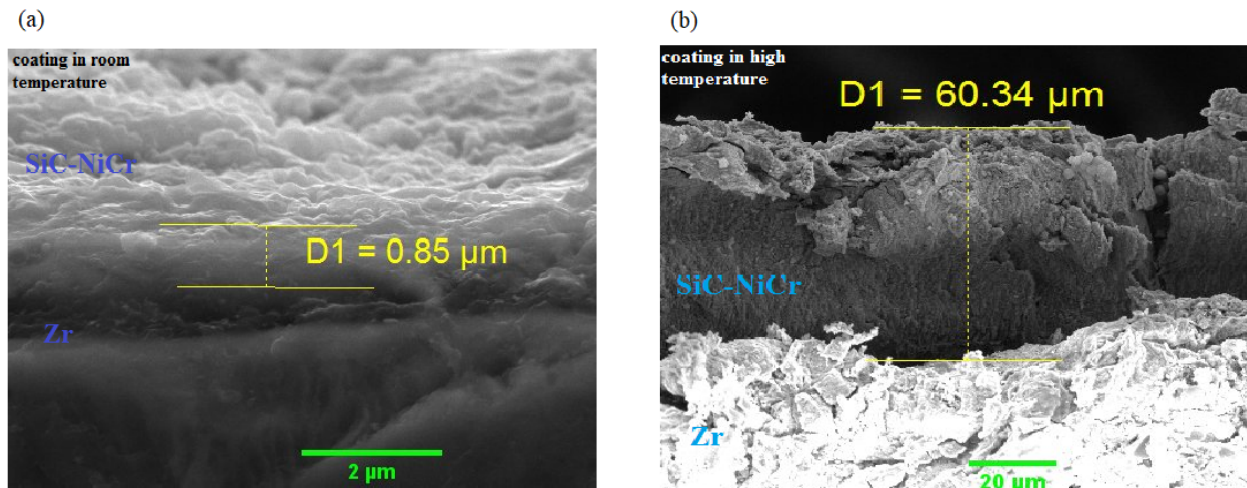


**Figure 5.** FESEM images of SiC−NiCr coating at high temperature (a) and room temperature (b).

**Figure 6.** Cross section images of SiC-NiCr thin films in (a) room temperature and (b) high temperature.

one or more monolayers, followed by the formation of islands. When the coated film and substrate are grown in this manner, a mismatched lattice may form. Based on the deposition temperature of the coated film on the substrate, the grain size of the film is determined [31]. The heating rate of the coating is 20º/min. A decrease in the heating rate is expected to cause the growth of the crystals formed on the surface, resulting in greater homogeneity of the layer between 25 and 1000 ºC. Reducing the weight percentage of Ni and Cr in the SiC−NiCr combination can also become one of the effective factors in achieving a homogeneous layer.

In the case of RT and high temperature, the average thickness of nanoparticles is 0.85 $\mu$m and 60.34 $\mu$m, respectively (Figs. 6a and b). The increased thickness improves the corrosion resistance of the SiC−NiCr coating on a Zr substrate at a temperature of 1000ºC. FESEM image of SiC−NiCr coating crack formation at 1000ºC is

shown in Figure 7. This coating has an estimated crack separation distance of 2.7 $\mu$m. Thermal treatment and other fabrication processes subject thin films to high residual stresses. On reaching critical values, these stresses, if tensile, result in cracks forming in the films. Thin films are often subjected to residual stresses when misfit strain $\varepsilon_0$ is applied to them. In the case of a film with a different thermal expansion coefficient than its substrate, the misfit strain will be biaxial and will measure the following:

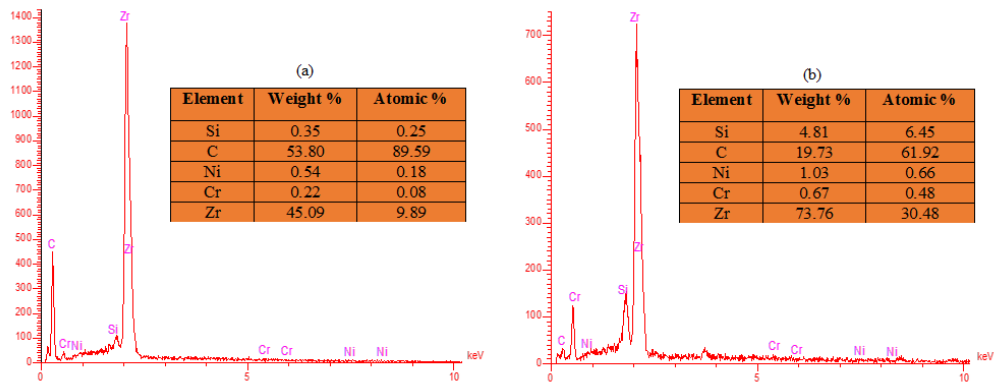$$\varepsilon_0 = (b_f - b_s)\Delta T \qquad (4)$$

$f$ indicates the film, while $s$ indicates the substrate, and $\Delta T$ indicates the temperature drop as well as $b$ indicates the thermal expansion coefficient.

Misfit stresses in films are also biaxial, with magnitudes of

$$\sigma_0 = \frac{\varepsilon_0 E_f}{1 - \nu_f} \qquad (5)$$
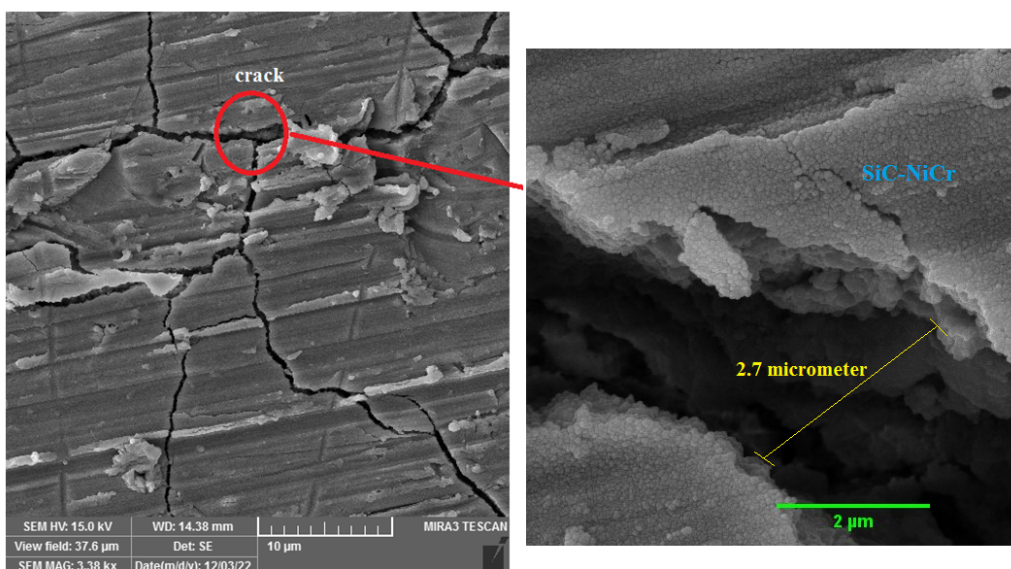


**Figure 7.** FESEM images of a crack formation on SiC-NiCr thin film deposited at 1000 ºC.

**Figure 8.** Energy dispersive X-ray of SiC-NiCr coating in (a) room temperature and (b) high temperature.

$E_f$ represents Young's modulus, and $\nu_f$ represents Poisson's ratio. The misfit strain and misfit stress were obtained as 0.0023, 0.67 Gpa, respectively (Table 4).

### 3.3  Energy-dispersive X-ray Spectroscopy (EDX)

An EDX analysis was conducted in order to determine the elements that make up the sample. Figure 8 illustrates the energy-dispersive X-ray image of the SiC-NiCr coating at RT and high temperature, together with the weight percentage of the coating on Zr. Zr and C exhibit high intensity peaks, as shown in Fig. 8. Particle degradation has been observed at 1000 ºC, resulting in a reduction in SiC in the coating. Alternatively, high temperatures promote the growth of Ni and Cr nanoparticles on Zr substrates.

### 3.4  Atomic force microscopy (AFM)

As a measure of surface roughness, a microscope of atomic force is employed in a non−contact state with a needle that has a diameter of less than 10 nm and a length of about 2 $\mu$m. Figures 9 illustrate AFM images of SiC-NiCr coating with DPF at RT and 1000 ºC on the Zr substrate with dimensions of 8.7 × 8.73 $\mu$m. As can be seen, the coating surface at 1000 ºC is smoother than the coating surface at RT. One of the reasons for this could be that the dispersion of nanoparticles is uniform at RT, but at 1000 ºC these nanoparticles coalesce and experience coaxial growth on the surface. In response to an increases in deposition temperature, changes in the size and density of crystal nuclei cause a significant change in the film morphology and surface roughness. According to figure 9a, SiC-NiCr coating at RT have average surface roughness ($R_a$), root mean square
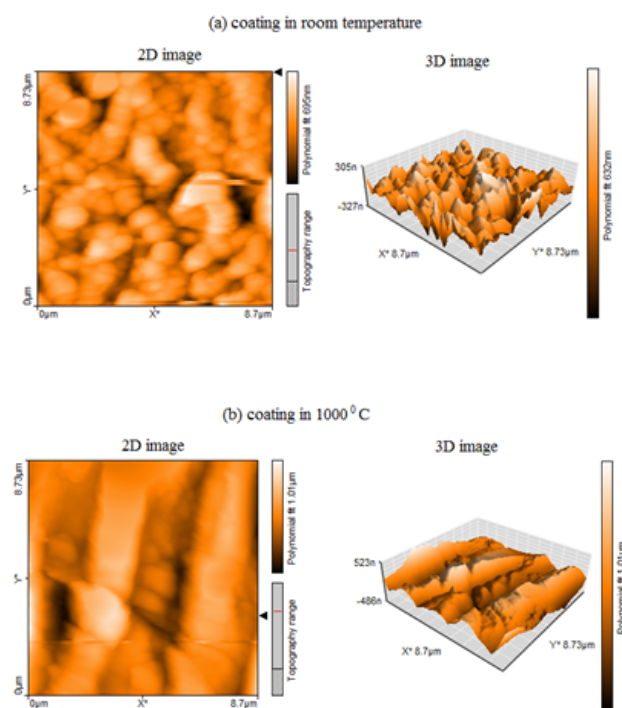


**Figure 9.** AFM images of SiC-NiCr thin films at (a) room temperature and (b) 1000 ºC.
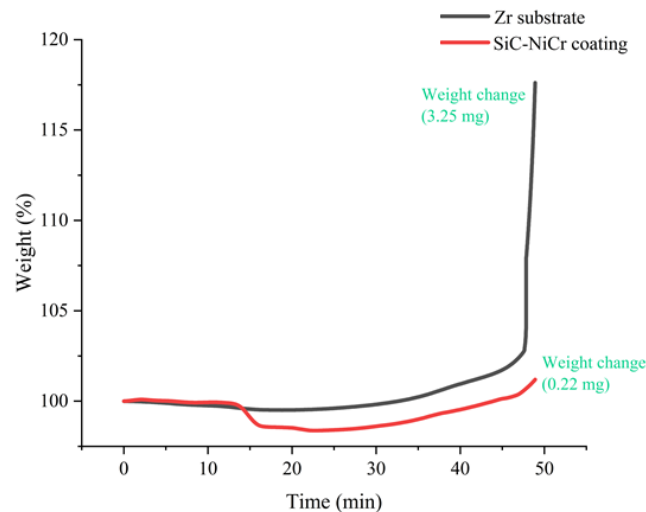
**Figure 10.** Graph of weight gain of Zr substrate and SiC-NiCr coating versus time at 1000 °C.

($R_q$) of 81.75 nm and 101.5 nm, respectively, and according to figure 9b, these quantities increased to 123.55 nm and 146.29 nm with increasing the temperature to 1000 °C.

## 4. Corrosion properties

### 4.1  Thermogravimetric analysis (TGA)
In a controlled environment, TGA determines how mass changes in response to temperature and time. This method involves placing the sample inside a plant and measuring the changes in the weight of the sample. A change in weight causes the magnetic core on the end of the wire to enter and exit the coil cylinder. In response to the movement of this core, an electric current corresponding to the change in weight of the sample is induced in the coil, and after being amplified, it is sent to the recording device. To measure the temperature of the sample, a thermocouple is placed near the bush where the sample is located. As part of the recording process, the vertical axis of the curve of changes in weight of the sample based on temperature changes is determined by the current induced in the coil, proportional to changes in weight, whereas the horizontal axis of the curve is determined by the electric current generated in the
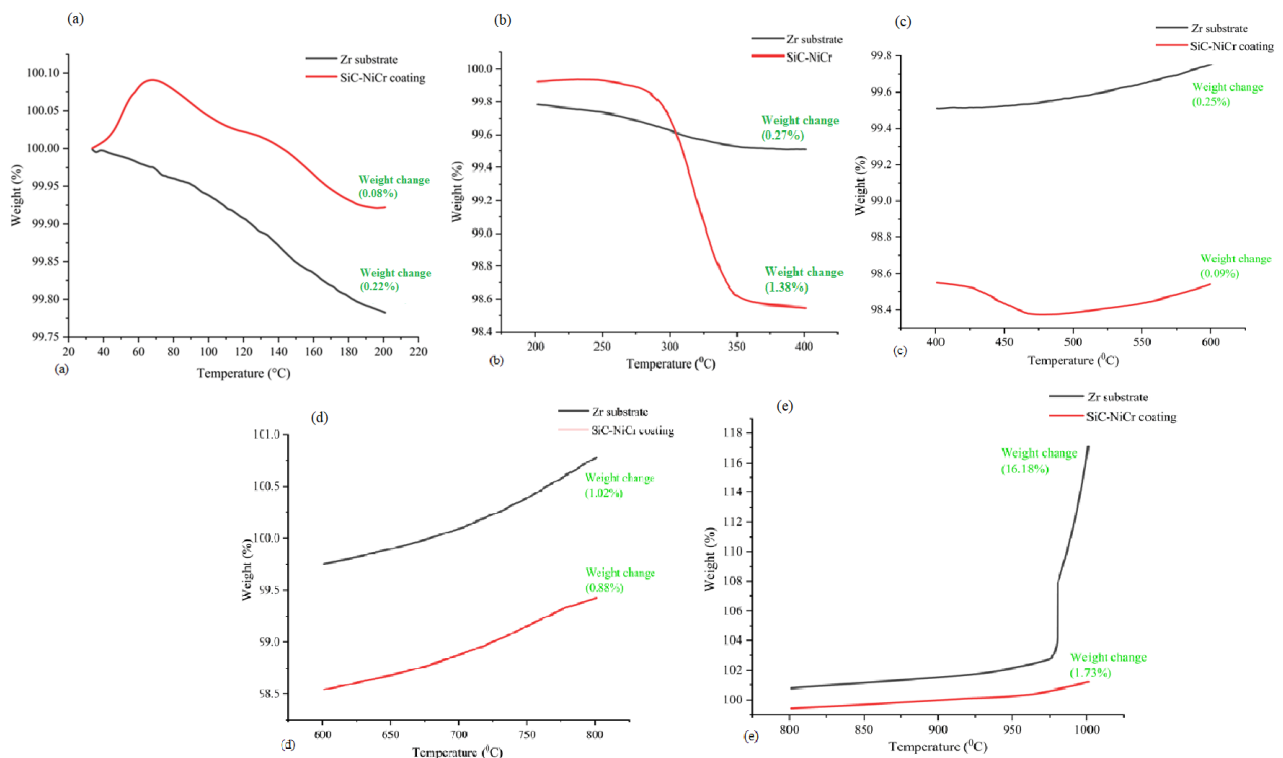


**Figure 11.** The graph of changes weight of the Zr substrate and SiC-NiCr coating versus temperature in a) 20 °C-200 °C, b) 200 °C-400 °C, c) 400 °C-600 °C, d) 600 °C-800 °C, and e) 800 °C-1000 °C.

thermocouple. Zr's corrosion behavior is assessed using the equation;

$$W = At^n, \qquad (6)$$

where $W$ represents the weight gain (%) and $t$ (min) represents the duration of the sample's exposure to the corrosive environment. Both $A$ and $n$ are constants. A number of factors, including transverse cracks and changes in the grain size of the oxide layer, will decrease the penetration rate in the oxide layer and will lower the value of $n$ as a result. As shown in Figure 10, the weight gain of Zr substrate and SiC-NiCr coating at 1000 ºC is plotted against time.

In comparison with the uncoated Zr, the SiC-NiCr coating resulted in a substantial decrease in weight gain (3.25 mg for substrate and 0.22 mg for SiC-NiCr coating). According to Figure 11a, the weight of the Zr substrate and the SiC-NiCr coating changes as the temperature changes from 200-1000 ºC. As the weight percentage changes during the course of the TGA curve, the first phase of decomposition begins at a lower temperature and progresses to a higher temperature. In the range of 20 ºC-200 ºC and 800 ºC-1000 ºC, the lowest and highest weight changes were observed, respectively. At 20 ºC-200 ºC, a decrease in mass is observed immediately after turning on the furnace and applying heat to the sample, which indicates that the raw material contains moisture (Fig. 11b). In the temperature range 200 ºC-400 ºC, the sample remains in a stable state when heated, and this state persists until it reaches a specific temperature, when the mass of the substance rapidly decreases, and the substance is once again in a stable state (Fig. 11b). By increasing the furnace temperature to 400 ºC-600 ºC and 600 ºC-800 ºC, the oxidation reaction between the sample and the surrounding atmosphere occurred, resulting in an increase in weight (Figs. 11c,11d). During high temperatures 800 ºC-1000 ºC, the substrate and coating undergo a significant weight change (16.8% and 1.73%, respectively), which may be caused by gas-solid reactions, oxidation, surface absorption, or internal absorption (Fig. 11e).

Corrosion rate ($CR$) is expressed as millimeters per year (mm/y) using weight changes $W$ as follows:

$$CR = \frac{km_{loss}}{\rho St} \qquad (7)$$

A constant value of $8.76 \times 10^4$ is used for $k$, and $CR$ is expressed in millimeters per year. $S$ is the area of the desired material, $\rho$ is the density of the material in gr/cm$^3$ and $m_{loss}$ is the loss of mass of the material in time $t$ (hours) [32].

During the corrosion process, the surface area changes with time as the objects dissolve in the corrosion environment. For uncoated and coated Zr substrates with SiC-NiCr, corrosion rates determined by TGA analysis and Eq. 6 as $1.31 \times 10^{-3}$ mm/year and $0.08 \times 10^{-3}$ mm/year, respectively.

## 5. Conclusions

Using a low-energy Plasma Focus Device, SiC-NiCr nanocomposites were grown on Zr substrates. In this experiment, 0.2 torr of pressure at 12 kV voltage was found to be the optimal pressure for the proper pinch. According to the XRD results, the peaks related to SiC at 1000 ºC in (111) and (022) crystallography planes and also, peaks related to diffraction of $Ni_4Cr_4O_{16}$ in (200), (112), (221), (113), (310), (311), and (241) crystallographic planes were observed. At higher temperatures, FESEM images show that the nanoparticle size and coating thickness increase. TGA analysis revealed that the most weight changes of the substrate and coating occurred at temperatures between 800 ºC and 1000 ºC. Based on TGA analysis and ASTM standards, the corrosion rate of Zr substrate without coating and coated with SiC-NiCr is $1.31 \times 10^{-3}$ mm/year and $0.08 \times 10^{-3}$ mm/year, respectively.

# References

[1] S. J. Zinkle and G. S. Was. "Materials challenges in nuclear energy". *Acta Mater.*, **61**:735–758, 2013.

[2] M. Shuichiro, Y. Yasunori, and Ch. Go. "Research activities on nuclear reactor physics and thermal-hydraulics in Japan after Fukushima-Daiichi accident". *J. Nucl. Sci. Technol*, **55**:575–598, 2018.

[3] L. J. Ott, K.R. Robb, and D. Wang. "Preliminary assessment of accident-tolerant fuels on LWR performance during normal operation and under DB and BDB accident conditions". *J. Nucl. Mater.*, **448**:520–533, 2014.

[4] M. Kurata. "Research and Development Methodology for Practical Use of Accident Tolerant Fuel in Light Water Reactors". *Nucl. Eng. Technol.*, **48**:26–32, 2016.

[5] T. Nishimura, H. Hoshi, and A. Hotta. "Current research and development activities on fission products and hydrogen risk after the accident at Fukushima Daiichi Nuclear Power Station". *Nucl. Eng. Technol.*, **47**:1–10, 2015.

[6] Z. Duan, H. Yang, Y. Satoh, K. Murakami, et al. "Current status of materials development of nuclear fuel cladding tubes for light water reactors". *Nucl. Eng.*, **316**:131–150, 2017.

[7] M. Hirano, T. Yonomoto, M. Ishigaki, N. Watanabe, et al. "Insights from review and analysis of the Fukushima Daiichi accident". *J. Nucl. Sci. Technol.*, **49**:1–17, 2012.

[8] F. Goldner. "USDOE Office of Nuclear Energy". *Washington*, , 2012.

[9] T. Matsunaka, K. Sasa, K. Sueki, T. Takahashi, et al. "Post-accident response of near-surface 129I levels and 129I/127I ratios in areas close to the Fukushima Daiichi Nuclear Power Plant". *Japan Nucl. Instrum. Methods Phys. Res.*, **361**:569–573, 2015.

[10] K. Hain, T. Faestermann, N. Famulok, L. Fimiani, et al. "Analytical method for the determination of Np and Pu in sea water by AMS with respect to the Fukushima accident". *Nucl. Instrum. Methods Phys. Res.*, **361**:505–509, 2015.

[11] Y. H. Koo, Y.S. Yang, and K. W. Song. "Radioactivity release from the Fukushima accident and its consequences: A review". *Prog. Nucl. Energy.*, **74**:61–70, 2014.

[12] E. Kashkarov, B. Afornu, D. Sidelev, M. Krinitcyn, et al. "Recent Advances in Protective Coatings for Accident Tolerant Zr-Based Fuel Claddings". *Coatings.*, **11**:557, 2021.

[13] K. A. Terrani, S. J. Zinkle, and L. L. Snead. "Advanced oxidation-resistant iron-based alloys for LWR fuel cladding". *J. Nucl. Mater.*, **448**:420–435, 2014.

[14] C. Tang, M. Stueber, H. J. Seifert, and M. Steinbrueck. "Protective coatings on zirconium-based alloys as accident tolerant fuel (ATF) claddings". *Corrosion reviews.*, **35**:141–165, 2017.

[15] B. Maier, H. Yeom, G. Johnson, T. Dabney, et al. "Development of Cold Spray Coatings for Accident-Tolerant Fuel Cladding in Light Water Reactors". *JOM.*, **70**:198–202, 2018.

[16] M. M. Larijani, M. Alijannejad, M. Yari, M. B. Zanjanbar, and M. Ghorannevis. "Study of carbon concentration on the nanostructural and corrosion properties of Zr(C, N)/ss304 films". *Eur. Phys. J. Appl. Phys.*, **50**:20501, 2010.

[17] S. H. Mohamed, N. M. A. Hadia, and Hazim Mahmoud Ali. "Effect of annealing on properties of decorative zirconium oxynitride thin films". *Eur. Phys. J. Appl. Phys.*, **69**:30301, 2015.

[18] D. Jin, F. Yang, Z. Zou, L. Gu, et al. "A study of the zirconium alloy protection by Cr3C2–NiCr coating for nuclear reactor application". *Surf. Coat. Technol*, **287**:55–60, 2016.

[19] T. Usui, A. Sawada, M. Amaya, A. Suzuki, et al. "SiC coating as hydrogen permeation reduction and oxidation resistance for nuclear fuel cladding". *Journal of Nuclear Science and Technology*, **52**:1–5, 2015.

[20] W. Bao, J. Xue, J. X. Liu, X. Wang, et al. "Coating SiC on Zircaloy-4 by magnetron sputtering at room temperature". *Journal of Alloys and Compounds*, **730**:81–87, 2018.

[21] Y. M. Lei, Y. H. Yu, C. X. Ren, S. C. Zou, et al. "Compositional and structural studies of DC magnetron sputtered SiC films on Si (111)". *Thin Solid Films*, **365**:53–57, 2000.

[22] L. S. Sig. "Thermal conductivity of liquid phase sintered silicon carbide". *J. Eur. Ceram. Soc.*, **23**:1115–1122, 2003.

[23] M. J. Suriani, W. B. W. Nik, F. Mansor, M. N. K. Jarkoni, et al. "Corrosion behavior and resistance parameters of silicon carbide nanocomposite coating on different metals". *Journal of Mechanical Engineering and Sciences*, **12**:3288–3301, 2018.

[24] Z.P. Wang, H. R. Yousefi, Y. Nishino, H. Ito, and K. Masugata. "Preparation of silicon carbide film by a plasma focus device". *Physics Letters.*, **372**:7179–7182, 2008.

[25] E. B. Kashkarov, M. S. Syrtanov, T. L. Murashkina, A. V. Kurochkin, et al. "Hydrogen Sorption Kinetics of SiC-Coated Zr-1Nb Alloy". *Coatings*, **9**:31, 2019.

[26] K. Bhanumurthy and R. S. Fetzer. "Interface reactions between silicon carbide and metals (Ni, Cr, Pd, Zr), Composites Part A". *Applied Science and Manufacturing.*, **32**:569–574, 2001.

[27] M. Hashim, M. Masoudi, H. M. Kamari, and M. S. Salit. "Fabrication and characterization of Ni–SiC–Cr nanocomposite coatings". *Appl Nanosci.*, **3**:357–362, 2013.

[28] V. D. Sidelev, E. B. Kashkarov, M. S. Syrtanov, and V. P. Krivobokov. "Nickel-chromium (Ni–Cr) coatings deposited by magnetron sputtering for accident tolerant nuclear fuel claddings". *Surface & Coatings Technology*, **369**:69–78, 2019.

[29] H. Anousha. "Properties of nanoscale copper oxide thin film deposited by plasma focus device". *Journal of Theoretical and Applied Physics*, **16**:1–10, 2022.

[30] H. Anousha and E. Ghareshabani. "Growth and characterization of TiAlN nanoparticles using low-energy plasma focus device". *Journal of Theoretical and Applied Physics*, **13**:231–235, 2019.

[31] O. O. Abegunde, E. T. Akinlabi, O. P. Oladijo, S. Akinlabi, and A. U. Ude. "Overview of thin film deposition techniques". *AIMS Materials Science*, **6**:174–199, 2019.

[32] ASTM Standard guide for laboratory immersion corrosion testing of metals. "ASTM International". *Thin Solid Films*, G31-12a:1–10, 2019.